

Ultrafast complete dechlorination enabled by ferrous oxide/graphene oxide catalytic membranes via nanoconfinement advanced reduction

Received: 10 April 2024

Accepted: 31 October 2024

Published online: 07 November 2024

 Check for updatesQian Xiao^{1,2,3}, Wanbin Li⁴ , Shujie Xie¹, Li Wang¹ & Chuyang Y. Tang^{1,5} 

Chlorinated organic pollutants widely exist in aquatic environments and threaten human health. Catalytic approaches are proposed for their elimination, but sluggish degradation, incomplete dechlorination, and catalyst recovery remain extremely challenging. Here we show efficient dechlorination using ferrous oxide/graphene oxide catalytic membranes with strong nanoconfinement effects. Catalytic membranes are constructed by graphene oxide nanosheets with integrated ultrafine and monodisperse sub-5 nm nanoparticles through simple in-situ growth and filtration assembly. Density function theory simulation reveals that nanoconfinement effects remarkably reduce energy barriers of rate-limiting steps for iron (III)-sulfite complex dissociation to sulfite radicals and dichloroacetic acid degradation to monochloroacetic acid. Combining with nanoconfinement effects of enhancing reactants accessibility to catalysts and increasing catalyst-to-reactant ratios, the membrane achieves ultrafast and complete dechlorination of $180 \mu\text{g L}^{-1}$ dichloroacetic acid to chloride, with nearly 100% reduction efficiency within a record-breaking 3.9 ms, accompanied by six to seven orders of magnitude greater first-order rate constant of $51,000 \text{ min}^{-1}$ than current catalysis. Meanwhile, the membranes exhibit quadrupled permeance of $48.6 \text{ L m}^{-2} \text{ h}^{-1} \text{ bar}^{-1}$ as GO ones, because nanoparticles adjust membrane structure, chemical composition, and interlayer space. Moreover, the membranes show excellent stability over 20 cycles and universality for chlorinated organic pollutants at environmental concentrations.

Haloacetic acids (HAAs) is an abundant group of disinfection by-products (DBPs) in water, whose maximum level could reach up to $600 \mu\text{g L}^{-1}$ in chlorinated drinking water¹. Dichloroacetic acid (DCAA), a dominant HAA, is one of the most widely produced DBPs in

chlorinated water². Inhalation or ingestion of DCAA can harm liver organs, as well as neurological and reproductive systems^{1,3}. It has been classified as a probable carcinogen to humans by the International Agency Research on Cancer^{3,4}. China and the United States have

¹Department of Civil Engineering, The University of Hong Kong, Hong Kong SAR 999077, China. ²State Key Laboratory of Pollution Control and Resource Reuse, College of Environmental Science and Engineering, Tongji University, Shanghai 200092, China. ³Shanghai Institute of Pollution Control and Ecological Security, Shanghai 200092, China. ⁴Guangdong Key Laboratory of Environmental Pollution and Health, College of Environment and Climate, Jinan University, Guangzhou 511443, China. ⁵Materials Innovation Institute for Life Sciences and Energy (MILES), HKU-SIRI, Shenzhen 518000, China.

 e-mail: gandeylin@126.com; tangc@hku.hk

regulated a maximum contamination level of $50 \mu\text{g L}^{-1}$ for DCAA and $60 \mu\text{g L}^{-1}$ for the sum of five HAAs including DCAA, monochloroacetic acid (MCAA), monobromoacetic acid (MBAA), dibromoacetic acid (DBAA), and trichloroacetic acid (TCAA) in drinking water^{2,5}. Furthermore, DCAA is of good water solubility, which facilitates its mobility in aquatic environments, rendering it difficult to be eliminated.

Several methods, including electrocatalytic^{6,7}, photochemical^{8–10}, and bulk catalytic^{11,12} technologies, have been proposed for decomposition of HAAs. However, these technologies often suffer from sluggish degradation process. Additionally, many existing methods result in incomplete dehalogenation (e.g., promoted formation of MCAA¹³). Sulfite (S(IV))-based advanced reduction processes (ARPs) are highly efficient in removing refractory halogenated organic contaminants and inorganic oxyanions, from bench to pilot studies^{14–18}. The ARPs generate reactive reducing species, such as sulfite radicals, and facilitate the cleavage of carbon-halogen bonds (i.e., C-Cl)^{19,20}. For catalysis, however, the decomposition rate ($\sim 0.15 \text{ s}^{-1}$) of transition metal ions-sulfite complexes was relatively slower^{16,21–24}. The energy-intensive separation (e.g., centrifugation)²⁵ for activation agents and the leached secondary pollutants (e.g., metal ions)²⁶ also hamper the practical application.

Catalytic membranes can integrate dual functions of filtration and catalysis^{27–30}. Membranes can harness catalysts and spatially confine reactants and active sites at the micrometer- and nanometer-scale, which offer the potential to enhance catalytic performance; meanwhile, catalysis can facilitate decomposition of contaminants that cannot be effectively rejected by membranes. To date, no study has combined ARPs and membrane separation, despite that great progress of catalytic membranes have been made in gas-phase reaction, organic degradation, as well as bulk/fine chemicals^{31,32}. Current catalytic membranes have been typically fabricated by anchoring catalysts onto ceramic and polymeric membranes through blending, surface coating, and bottom-up synthesis³³. These approaches often led to the dropping and deactivation of catalysts, ineffective dispersion of catalyst particles, and degradation of catalytic membranes^{33,34}. Graphene oxide (GO) surfaces contain an abundance of functional groups, thereby facilitating catalyst loading and mitigating nanoparticle (NP) aggregation. We, thus, posit designing ultrafine iron-based NP/graphene oxide composite membranes for advanced reduction of HAAs, which provide nanoconfinement effects to achieve reduced activation energy for the formation of reducing radicals for DCAA dechlorination. Furthermore, the reductants, including S(IV) and contaminants, must undergo nanoconfined transport through the catalyst-loaded interlayer channels of the iron-based NP/graphene oxide composite membranes. This greatly enhances the reductant-catalyst contact probability compared to the bulk solution based catalysts. Additionally, the catalysts and reactions will be nanoconfined in the interlayer transport nanochannels of GO membranes, which will substantially increase the catalyst-to-reactant ratios in confined reaction regions and then promote contaminant degradation.

In this study, we report efficient dechlorination of DCAA through constructing catalytic membranes by deposition of ultrafine FeO NPs on GO nanosheets. Through simple in-situ growth, monodispersed sub-5 nm FeO NPs can be deposited on oxygen functional groups of GO. The Fe/GO membranes possess ultrafast degradation performance of DCAA to chloride, with a nearly 100% removal within a record-breaking 3.9 ms, accompanied by a six to seven orders of magnitude greater first-order rate constant of $51,000 \text{ min}^{-1}$ than conventional processes ($0.0013 - 33.3 \text{ min}^{-1}$), which can be attributed to enhanced reactants accessibility to catalytic sites, increased catalyst-to-reactant ratios in reaction regions, and reduced activation energy induced by nanoconfinement effects for FeSO_3^+ dissociation into sulfite radicals and for DCAA dechlorination. Meanwhile, the Fe/GO membranes give a quadruple water permeance of $48.6 \text{ L m}^{-2} \text{ h}^{-1} \text{ bar}^{-1}$ as GO ones, due to the adjustment of FeO NPs to oxidation degree,

interlayer space, and membrane structure. Moreover, the prepared membranes exhibit excellent stability with maintained performance over 20 cycles and great universality for dehalogenation and reduction of other HAAs (>97%) and chlorinated organic pollutants (>90%).

Results

In-situ growth of Fe/GO nanosheets

We synthesized the Fe/GO composite nanosheets through in-situ growth of FeO NPs by introducing a 1.5 mmol L^{-1} FeCl_3 solution (20 mL) to the GO suspension (20 mg L^{-1} , 150 mL) and reduction of Fe^{3+} by NaBH_4 (1.6 M, 75 μL). The electronegative oxygen functional groups of GO adsorbed Fe^{3+} ions, and then FeO NPs would be preferentially and heterogeneously nucleated at active sites under NaBH_4 reduction. FeO NPs were obtained by introducing NaBH_4 to reduce the Fe^{3+} ions that are adsorbed onto the GO. Transmission electron microscopy (TEM) and scanning transmission electron microscopy (STEM) images show monodispersed sub-5 nm NPs with a high number density of $\sim 2 \times 10^5 \text{ m}^{-2}$ on the $\text{Fe}_{\text{CLs}}/\text{GO}$ nanosheets (Fig. 1a–d and Supplementary Fig. 1). High-resolution TEM image indicated the presence of lattices with space of 2.54 and 2.15 Å, which are assigned to the (111) and (200) facets of FeO, respectively (Fig. 1c, inset). Electron diffraction implied that the NPs were FeO with exposed facets of (111), (200), (220), and (222) (Fig. 1d, inset). Energy-dispersive X-ray spectroscopy (EDS) analysis revealed the presence of elemental Fe and O (Fig. 1e, f), indicating successful in-situ growth and uniform dispersion of FeO NPs throughout the GO. As shown in the atomic force microscopy (AFM) image (Fig. 1g), the GO nanosheets were single-layered with a thickness of 1.0 nm, while the single-layered $\text{Fe}_{\text{CLs}}/\text{GO}$ nanosheets had slightly rougher surface than GO due to the attachment of ultrasmall NPs (Fig. 1h).

X-ray photoelectron spectroscopy (XPS) analysis was carried out to study the chemical binding states. Relative to GO with a C/O ratio of 2.42, the $\text{Fe}_{\text{CLs}}/\text{GO}$ nanosheets exhibited a higher C/O ratio of 3.27, despite the existence of O in FeO, suggesting the reduction of GO after in-situ growth of FeO. In addition to the two main peaks of C and O in the XPS spectrum, a new Fe peak was observed in the XPS spectrum of $\text{Fe}_{\text{CLs}}/\text{GO}$, with the atomic content of 0.75%. High-resolution XPS spectra indicated that Fe existed as FeO and Fe_2O_3 , with contents of 53.6% and 46.4%, respectively (Fig. 1i). No obvious peaks were observed for zero-valent iron. High-resolution C 1s spectra of GO and $\text{Fe}_{\text{CLs}}/\text{GO}$ could be deconvoluted into three peaks of sp^3 hybridized carbon atoms at 284.8 eV, hydroxyl and epoxy at 287.1 eV, and carbonyl and carboxyl at 288.2 eV (Fig. 1j)^{35–37}. Consistent with the variation in the C/O ratio, the contents of C–O and C=O declined from 36.1% and 12.5% for GO to 22.4% and 10.2% for $\text{Fe}_{\text{CLs}}/\text{GO}$, respectively, suggesting the reduction of GO after in-situ growth. Notably, the GO after immersion in NaBH_4 (reducing agent) solution without FeCl_3 displayed only slight variations in the C/O ratio and oxygen-containing group content (Supplementary Fig. 2). This phenomenon implied that FeCl_3 might play an important role in promoting the reduction of GO, potentially by the involvement of Fe^{3+} as electron shuttling, which was facilitated through the electrostatic adsorption between Fe^{3+} and negatively charged GO sheets. Raman spectroscopy was used to investigate the regularity of nanosheet structures. Obviously, the spectra of GO and $\text{Fe}_{\text{CLs}}/\text{GO}$ showed two peaks of D (1322 cm^{-1}) and G (1592 cm^{-1}) bands, which were ascribed to the breathing vibration of defect/disordered sp^3 and the in-plane stretching vibration of original sp^2 , respectively³⁸. Compared to GO with ID/IG ratio of 1.32, the $\text{Fe}_{\text{CLs}}/\text{GO}$ nanosheets were slighter disorder with a lower ID/IG ratio of 1.21 owing to the reduction, which agreed with the XPS results.

Besides $\text{Fe}_{\text{CLs}}/\text{GO}$ prepared with a FeCl_3 concentration of 1.5 mmol L^{-1} , the Fe/GO nanosheets were synthesized with other precursor concentrations. For the nanosheets prepared with FeCl_3 concentrations of 0.5 and 1.0 mmol L^{-1} , i.e., $\text{Fe}_{\text{C0.5}}/\text{GO}$ and $\text{Fe}_{\text{C1.0}}/\text{GO}$, the Fe atomic content was 0.40% and 0.60%, respectively, lower than that of

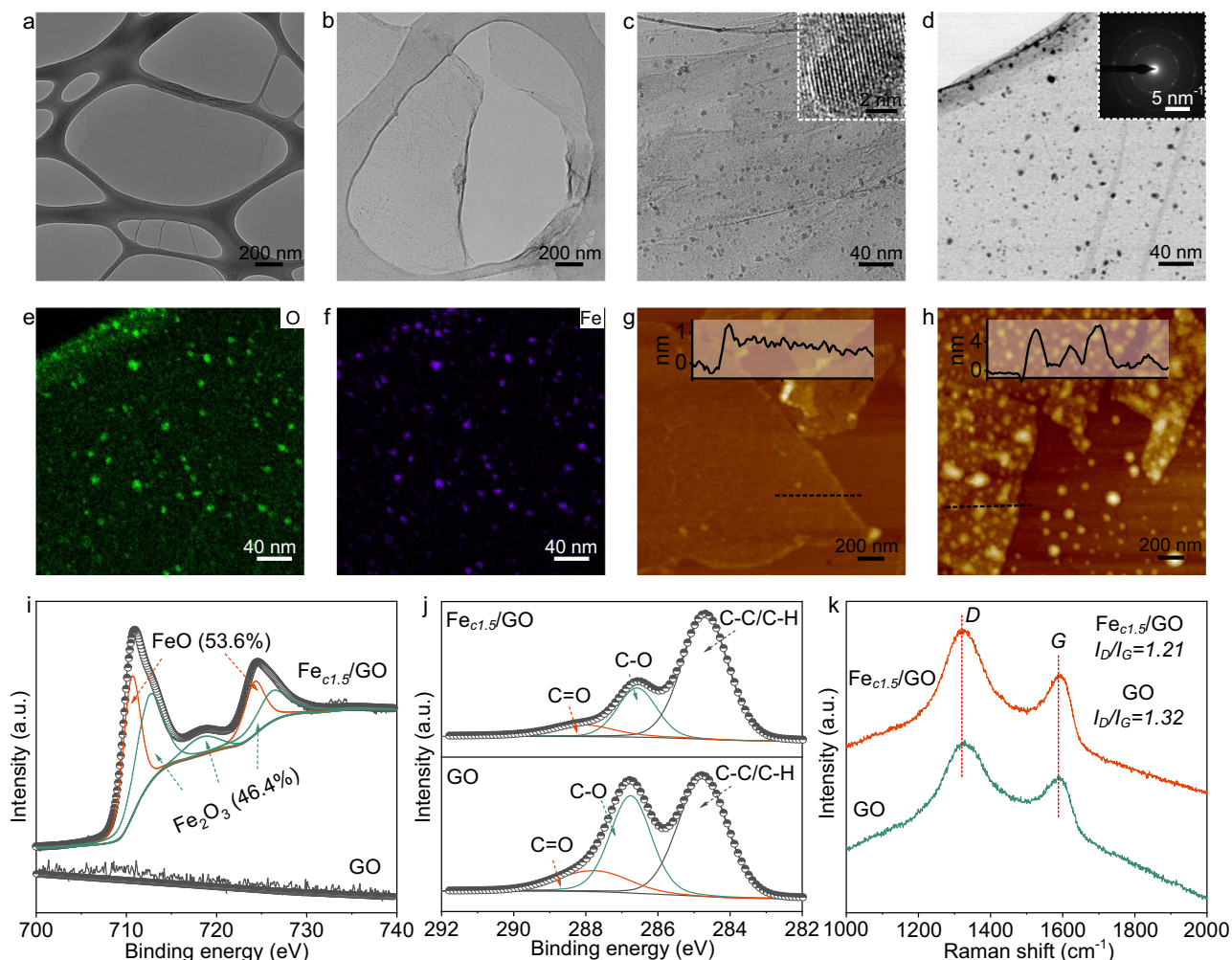


Fig. 1 | Characterizations of Fe/GO nanosheets. **a** TEM image of a typical GO nanosheet. **b, c** TEM image of a typical $\text{Fe}_{\text{cl,s}}/\text{GO}$ nanosheet. Inset presents the TEM image of FeO NPs on nanosheet. **d** STEM image of a typical $\text{Fe}_{\text{cl,s}}/\text{GO}$ nanosheet. Inset presents electron diffraction. **e, f** EDS mapping images of the $\text{Fe}_{\text{cl,s}}/\text{GO}$

nanosheet. **g, h** AFM images of the GO and $\text{Fe}_{\text{cl,s}}/\text{GO}$ nanosheets. Inset presents height profiles. **i**, Fe 2p XPS spectra of GO and $\text{Fe}_{\text{cl,s}}/\text{GO}$. The proportions of Fe(II) and Fe(III) were estimated based on the peak areas. **j** C 1s XPS spectra of GO and $\text{Fe}_{\text{cl,s}}/\text{GO}$. **k** Raman spectra of GO and $\text{Fe}_{\text{cl,s}}/\text{GO}$. a. u. represents arbitrary unit.

$\text{Fe}_{\text{cl,s}}/\text{GO}$. As expected, the C/O ratio, oxygen-containing group content, and structural regularity fell between those of GO and $\text{Fe}_{\text{cl,s}}/\text{GO}$, as identified by XPS and Raman results (Supplementary Figs. 3–5). For the nanosheets synthesized with concentrations $>1.5 \text{ mmol L}^{-1}$, the excessive loading induced the formation of defects in the Fe/GO membranes, as demonstrated below.

Construction of Fe/GO membranes

After in-situ growth of FeO NPs, the Fe/GO nanosheets were filtrated onto a polyvinylidene difluoride substrate with a pore size of $0.22 \mu\text{m}$ to fabricate the Fe/GO membranes (Supplementary Fig. 6). Photographs indicated that the nanosheets uniformly covered the substrates, and membranes with higher FeO loadings appeared darker (Supplementary Fig. 7). The GO and $\text{Fe}_{\text{cl,s}}/\text{GO}$ membranes were uniform, defect-free, and ultrathin, with the thickness $<100 \text{ nm}$ (Fig. 2a–d). Some wrinkles appeared on the GO membrane due to nanosheet flexibility, and the wrinkles of the Fe/GO membranes were weakened as loading increased (Fig. 2a, c, e, f and Supplementary Fig. 8). This phenomenon was explained by that the FeO growth reduced the flexibility of nanosheets, which might be beneficial to immobile the mass transfer channels during filtration under pressure and then maintain permeation properties. We prepared the Fe/GO membranes with higher loadings over 1.5 mmol L^{-1} (Supplementary Fig. 9), but

many defects were generated in these membranes, because small nanosheet flexibility and excessive FeO loading caused irregular stacking. Top and cross-sectional view EDS mapping images revealed the homogeneous iron distribution throughout the Fe/GO membranes (Fig. 2g, h).

For GO membranes, the interlayer space is not only dominant transport channels for permeation, but provides sites for the confined reaction³⁹. We studied the crystalline structure and interlayer space of the prepared membranes. From the X-ray diffraction (XRD) patterns (Fig. 2i), it could be seen that the diffraction peak for (002) plane of the GO membrane was located at 10.6° , which was consistent with previously reported value⁴⁰. After in-situ growth, the peak of the Fe/GO membranes shifted to a lower degree due to the insertion of FeO NPs and became lower as the loading increased, e.g., 9.5° for $\text{Fe}_{\text{cl,s}}/\text{GO}$. According to the Bragg's law, the interlayer spaces of GO and $\text{Fe}_{\text{cl,s}}/\text{GO}$ were 8.3 and 9.3 \AA , respectively. Besides the dry state, the membranes were immersed in water for 1 h to investigate the interlayer space under wetted state. Compared with that under the dry state, the diffraction degrees of the GO and Fe/GO membranes became smaller (Fig. 2j), due to the hydration of nanosheets from the affinity of oxygen-containing groups towards water molecules. For example, the diffraction angles of the wetted GO and $\text{Fe}_{\text{cl,s}}/\text{GO}$ membranes decreased to 6.6° and 5.8° , respectively. Under the wetted state, the

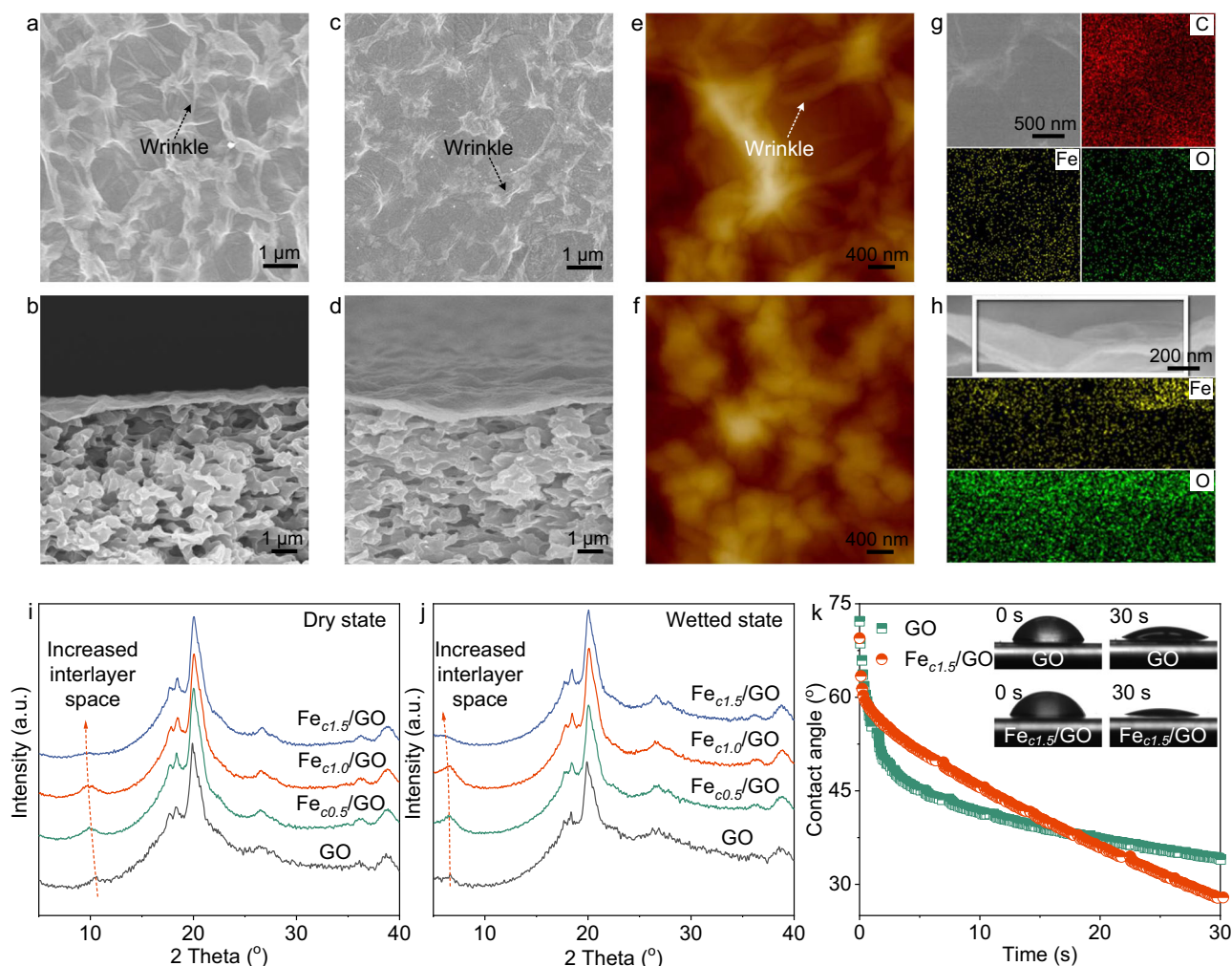


Fig. 2 | Characterizations of Fe/GO membranes. **a, b** Top and cross-sectional view SEM images of the GO membrane. **c, d** Top and cross-sectional view SEM images of the Fe_{c1.5}/GO membrane. **e, f** AFM images of the GO and Fe_{c1.5}/GO membranes. **g, h** Top and cross-sectional EDS mapping images of the Fe_{c1.5}/GO membrane. **i** XRD

patterns of the Fe/GO membranes fabricated with different Fe precursor concentrations at dry state. **j** XRD patterns of the Fe/GO membranes fabricated with different Fe precursor concentrations at wetted state. a. u. represents arbitrary unit. **k** Dynamic water contact angle of the GO and Fe_{c1.5}/GO membranes.

Fe/GO membranes also had smaller diffraction angles and larger interlayer space than GO, and the interlayer space became wider as FeO loading increased, from 13.3 Å for GO to 15.2 Å for Fe_{c1.5}/GO. Apart from the interlayer space, the dynamic water contact angles of the GO and Fe_{c1.5}/GO membranes were measured (Fig. 2k). Due to the reduction of GO, the contact angle of Fe_{c1.5}/GO was slightly larger than that of GO at the beginning, yet its decline over time was faster as the FeO deposition enhanced the water transport through the Fe_{c1.5}/GO layers. Overall, the enhanced hydrophilicity of Fe_{c1.5}/GO could remarkably promote the interactions between FeO and aqueous solutions, and thus water dehalogenation.

Performance of Fe/GO membranes

We evaluated the performance of the membranes for DCAA degradation in the presence of 1.0 mM S(IV). The permeance became larger with increased FeO loading (Fig. 3a), which can be attributed to the increase in interlayer space from the FeO insertion and the decrease of oxygen functional groups from reduction⁴¹. For example, the Fe_{c1.5}/GO membrane exhibited quadrupled permeance compared to that of GO, reaching up to 48.6 L m⁻² h⁻¹ bar⁻¹. Interestingly, the reduction efficiency increased simultaneously. For Fe_{c1.5}/GO, the efficiency was 96.8%, much > 36.2% for GO. Notably, the Fe/GO membrane fabricated with Fe precursor over 1.5 mmol L⁻¹ exhibited poor reduction efficiency

(<10%) due to the existence of defects (Supplementary Fig. 9). Therefore, the Fe_{c1.5}/GO membrane was chosen for the subsequent experiments. Figure 3b illustrated that the DCAA reduction was accompanied by the Cl⁻ formation, indicating that Cl⁻ was the only Cl-containing product.

We measured the DCAA reduction efficiency under various processes to investigate the roles of S(IV) and FeO. A nearly complete removal of DCAA could be achieved for the Fe_{c1.5}/GO membrane in the presence of 1.0 mM S(IV) (Fig. 3c). In contrast, only S(IV) addition exerted little effect on the removal of DCAA, since S(IV) did not generate active radicals via self-decomposition⁹. In the absence of S(IV), the Fe_{c1.5}/GO membrane exhibited a removal efficiency of only 35.5–50.7%. Since no chlorine-containing product detected in the permeate, this partial removal was likely due to the adsorption in nanochannels. Additionally, the GO membrane without FeO showed a low removal efficiency of 36.2% within 60 min in the presence of 1.0 mM S(IV), suggesting the importance of iron sites in Fe/GO membranes for S(IV) activation and further reduction processes. Furthermore, an additional FeO/GO membrane was synthesized by filtering commercial FeO nanoparticles (20 nm) onto the GO membrane. This composite membrane showed a removal efficiency of 45.6% in the presence of 1.0 mM S(IV) (Fig. 3c). However, the ultrafast DCAA degradation was only observed in Fe/GO membrane catalytic systems,

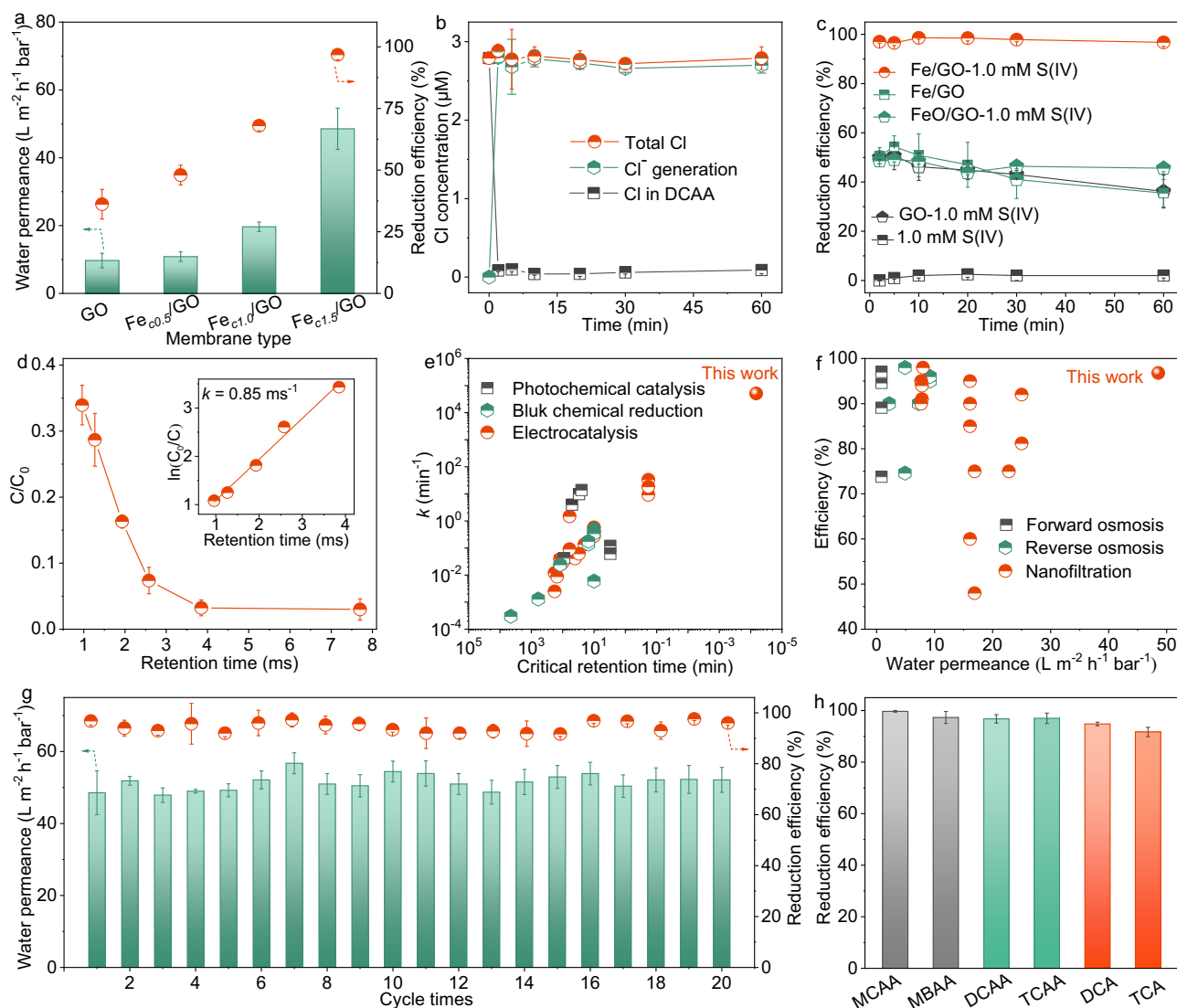


Fig. 3 | Performance of Fe/GO membranes. **a** Water permeance and DCAA reduction efficiency of Fe/GO membranes as a function of iron loading amounts. Conditions of the feed solution: initial DCAA level = $180 \mu\text{g L}^{-1}$, initial S(IV) level = 1.0 mM , pH_{ini} , 7.0 ± 0.1 , and $25 \pm 0.5^\circ \text{C}$. **b** Cl-containing product and the mass balance of the total Cl in $\text{Fe}_{\text{CL}/\text{S}}$ /GO membranes/S(IV) systems. Conditions of the feed solution: initial DCAA level = $180 \mu\text{g L}^{-1}$, pH_{ini} , 7.0 ± 0.1 , and $25 \pm 0.5^\circ \text{C}$. **d** Normalized concentration of DCAA (C/C_0) versus membrane retention time. Retention time indicates the ratio of the pore volume within the catalytic membrane over the flow rate through the membrane. As shown in Eq. 1 in the methodology according to a previous study³⁹, it can be experimentally controlled by adjusting the applied pressure. **e** Comparison

of first-order rate constant (k) values. Critical retention time indicates the time for achieving > 90% of removal (Supplementary Table 1). **f** Comparison of permeance and removal efficiency between our Fe/GO membrane and other nanofiltration, forward osmosis, and reverse osmosis membranes (Supplementary Table 2). **g** Stability test of water permeance and reduction efficiency over cycle times. **h** Reduction efficiency of four HAAs and two chlorinated organic pollutants. Conditions of the feed solution: initial level of each HAA = $180 \mu\text{g L}^{-1}$, initial levels of DCA and TCA = 0.5 mM , initial S(IV) level = 1.0 mM , pH_{ini} , 7.0 ± 0.1 , and $25 \pm 0.5^\circ \text{C}$. Error bars represent the standard deviation from at least triplicate experiments. Some of the error bars are smaller than the symbols.

where Fe NPs were loaded in the interlayer spaces of GO, indicating that FeO needs to be placed within a confined space to enhance contact between reactants with FeO, and to decrease energy barriers associated with S(IV) activation and DCAA reduction for achieving unprecedented degradation performance.

Generally, degradation of HAAs is regarded as first-order reactions^{42,43}. The calculated first-order rate constant for reducing DCAA by the $\text{Fe}_{\text{CL}/\text{S}}$ /GO membrane reached $51,000 \text{ min}^{-1}$ (0.85 ms^{-1}) (Fig. 3d), which was six to seven orders of magnitude greater than that by electrocatalytic process ($0.0025 - 33.3 \text{ min}^{-1}$), photochemical system ($0.042 - 13.9 \text{ min}^{-1}$), and bulk chemical reduction ($0.0013 - 0.5 \text{ min}^{-1}$) (Fig. 3e and Supplementary Table 1). Meanwhile, the $\text{Fe}_{\text{CL}/\text{S}}$ /GO membrane required an extremely short

retention time of a record-breaking 3.9 ms for nearly complete DCAA reduction. By contrast, it would take up to ~600 hrs to achieve the same reduction level in bulk solutions spiked with 50 mg of Fe/GO nanosheets (i.e., 0.5 g L^{-1}) (Supplementary Fig. 10). Besides, in comparison with catalytic systems, the performance of the $\text{Fe}_{\text{CL}/\text{S}}$ /GO membrane could also easily break the trade-off limitation between water permeability and removal efficiency of membrane separation processes, including nanofiltration, forward osmosis, and reverse osmosis (Fig. 3f and Supplementary Table 2). This high permeability of Fe/GO membranes was attributable to the expanded interlayer space from FeO intercalation and the decreased friction from removal of functional groups⁴⁴. Notably, the $\text{Fe}_{\text{CL}/\text{S}}$ /GO membrane could achieve >90.8% DCAA

dechlorination for tap water samples with environmentally relevant DCAA concentrations (i.e., $80 \mu\text{g L}^{-1}$) (Supplementary Fig. 11).

In addition to permeance and degradation efficiency, the stability and universality of the Fe/GO membrane catalytic system were further investigated through pressure-dependent continuous cross-flow experiments. As presented in Fig. 3g, the $\text{Fe}_{\text{c.l.s.}}/\text{GO}$ membrane showed nearly unchanged water permeance and DCAA reduction efficiency over 20 cycle times (with each cycle lasting ~1 h). Meanwhile, the amount of Fe leached during reduction was below the detection threshold of $1.0 \mu\text{g L}^{-1}$ (Supplementary Fig. 12). Furthermore, the chemical composition of $\text{Fe}_{\text{c.l.s.}}/\text{GO}$ membrane samples before and after cyclic test was assessed by conducting the Fe XPS analysis. Less than 2.3% Fe(II) in the $\text{Fe}_{\text{c.l.s.}}/\text{GO}$ membrane was converted into Fe(III) after operation for 20 hrs (Supplementary Fig. 13), indicating the excellent stability of catalytic sites and the efficient conversion of Fe(II)/Fe(III). Reportedly, Fe(II) exhibits a greater ability for activating S(IV) compared to Fe(III)^{16,21–24}; specially, Fe(II) provides electrons to facilitate the formation of Fe(III)-sulfite complexes, and decomposition of these complexes results in the production of Fe(II), with Fe(III) being the immediate that complexes with sulfite. The relatively stable distribution weight of Fe(II) through facilitated electron shuttling likely by the electrically conductive reduced graphene oxide (rGO), further promoted S(IV) activation and DCAA reduction. All above results demonstrated the great stability of the Fe/GO membrane and was attributed to the stably confined FeO NPs within the GO nanosheets. To confirm the generic applicability, the $\text{Fe}_{\text{c.l.s.}}/\text{GO}$ membrane was used to remove a diverse range of pollutants, including haloacetic acids (i.e., MCAA, MBAA, DCAA, and TCAA) and chlorinated organic pollutants (i.e., 1,2-dichloroethane (DCA) and 1,1,1-trichloroethane (TCA)). All the pollutants were rapidly and almost completely reduced (Fig. 3h), with the primary degradation products of halogen ions (i.e., Cl^- and Br^-) (Supplementary Fig. 14). Overall, the $\text{Fe}_{\text{c.l.s.}}/\text{GO}$ membrane could perform a robust ARP with great performance, excellent stability, and universal applicability.

Mechanisms of confinement catalysis and high permeability

Three main reasons can be utilized to explain ultrahigh reduction efficiency. Firstly, nanoconfinement effects enhance reactants accessibility to catalysts. During the Fe/GO membrane catalysis, to reach the permeate side, all reactants including S(IV) and DCAA had to pass the nanoconfined transport channels between adjacent GO nanosheets, which had been loaded with high-density Fe NPs, consequently largely increasing reactants accessibility to catalysts for accelerating DCAA decomposition. Secondly, nanoconfinement effects increase catalyst-to-reactant ratios (Supplementary Text 1 and Supplementary Table 3). All Fe NPs were loaded in the GO interlayer nanochannels, the reaction regions were nanoconfined as well, thereby substantially increasing catalyst-to-reactant ratios in reaction regions for promoting S(IV) complexation and electron transfer^{16,21–24} and thus enhancing S(IV) activation and contaminant degradation. In fact, the effective molar ratios of Fe to sulfite and Fe to DCAA reached as high as 1168–292 and 418963–104741, respectively (see detailed calculation in Supplementary Text 1), which were much higher than those for catalysis in bulk solution (i.e., 0.1–0.5 and 5–20, respectively^{15,16,45,46}). Thirdly, nanoconfinement effects greatly reduce energy barrier. Nanoconfinement effects for adjacent GO nanosheets would significantly reduce the energy barrier and facilitate the removal of contaminants, which was demonstrated by density function theory (DFT) simulation as below.

We investigated the energy profile of S(IV) activation within Fe/GO membranes and on FeO NPs using DFT calculations. The activation process of S(IV) falls into three stages: (1) adsorption of S(IV) on FeO surfaces, resulting in the formation of iron(II)-sulfite complex (FeHSO_3^+); (2) oxidation of FeHSO_3^+ to iron(III)-sulfite complex (FeSO_3^+) in the presence of O_2 ; (3) decomposition of FeSO_3^+ , leading to the formation of sulfite radicals ($\text{SO}_3^{\cdot-}$) (Fig. 4a). Amongst these stages,

the generation of $\text{SO}_3^{\cdot-}$ through the decomposition of FeSO_3^+ was the rate-limiting step. Figure 4a indicated a remarkable decline in the kinetic free-energy barrier for the dissociation of FeSO_3^+ into $\text{SO}_3^{\cdot-}$ (from 0.41 to 0.86 eV) through Fe/GO, compared to FeO (from -1.44 to 0.86 eV). It further resulted in higher formation of $\text{SO}_3^{\cdot-}$ ($\alpha_{\text{N}}=14.7$, $\alpha_{\text{B-H}}=16.0$) for Fe/GO spiked with S(IV) in comparison with FeO/S(IV) (Fig. 4b), implying an important role of spatial confinement of GO matrix towards FeO in S(IV) activation.

We calculated the length of the C-Cl bond for Fe/GO, FeO, GO, and a free environment (Supplementary Fig. 15). Longer length of C-Cl means more easily degradation. The calculated length of the C-Cl bond for Fe/GO and FeO was 1.807 and 1.829 Å, respectively, which was 0.018–0.069 Å longer than the normal C-Cl bond for GO membranes (1.789 Å) and a free DCAA molecule (1.760 Å), suggesting that iron active sites can bind DCAA and intermediates. From the energy profiles associated with the degradation of DCAA by Fe/GO and FeO in the presence of S(IV), it was obvious that the conversion of CHCl_2COOH to CH_2ClCOOH was the rate-limiting step (Fig. 4c). Compared to FeO (-0.49 eV to 2.02 eV), Fe/GO required the lower kinetic free-energy barrier associated with the transformation of CHCl_2COOH into CH_2ClCOOH , from -0.57 eV to 1.67 eV, in the presence of S(IV). These processes would undergo a remarkable amplification by a combination of the spatial confinement during the activation of S(IV). These results indicated that confinement effects remarkably reduced the energy for the rate-limiting steps, i.e., FeSO_3^+ dissociation into sulfite radicals in activation process and CHCl_2COOH transformation into CH_2ClCOOH in degradation process, together favoring the reduction of DCAA and reaction intermediates on the iron centers through Fe/GO membranes.

Apart from great reduction efficiency, for water permeation of GO membranes, the molecules pass through defects/edges of nanosheets and interlayer spaces between adjacent nanosheets^{47,48}. Due to the two-dimensional configuration, the interlayer channels primarily govern the permeance of GO membranes. We calculated the diffusion processes of water molecules through the interlayer space of GO and Fe/GO membranes using molecular dynamic (MD) simulations. Results in Fig. 4d, e showed that the diffusion constant for the Fe/GO membrane was $1.58 \times 10^{-5} \text{ cm}^2 \text{ s}^{-1}$, larger than $1.21 \times 10^{-5} \text{ cm}^2 \text{ s}^{-1}$ for GO. This difference could be attributed to the expanded interlayer space from 13.3 Å for GO to 15.2 Å for $\text{Fe}_{\text{c.l.s.}}/\text{GO}$. Meanwhile, the higher density of water on GO than on Fe/GO from the more oxygen-containing groups implied the greater interaction, thereby reducing water diffusion process (Supplementary Fig. 16). In other words, the friction experienced by water molecules within the interlayer spaces of Fe/GO membranes was lower than that within GO. However, the diffusion constant ratio of Fe/GO to GO was 123%, lower than the quadruple permeance ratio observed in experimental results. Although molecular transports were heavily affected by interlayer channels, the free spaces within GO membranes, resulting from irregular stacking and nanoparticle insertion, could provide transport channels and reduce tortuosity to enhance water permeance⁴⁹. Benefiting from the insertion of FeO NPs, a considerable number of free spaces would be formed, thereby further improving water permeance.

Discussion

We have constructed the Fe/GO membranes with uniform FeO NPs and proved their great performance for dechlorination. Because of enhanced reactants accessibility to catalytic sites, increased catalyst-to-reactant ratios in reaction regions, and promoted activation of FeSO_3^+ to sulfite radical and conversion of DCAA to MCAA, the membranes show great reduction efficiency for degradation of DCAA to chloride, with a first-order rate constant of $51,000 \text{ min}^{-1}$, which is six to seven orders of magnitude greater than conventional catalytic systems. Because of the adjustment from the growth of FeO NPs to membrane structure, chemical composition, and interlayer space, the

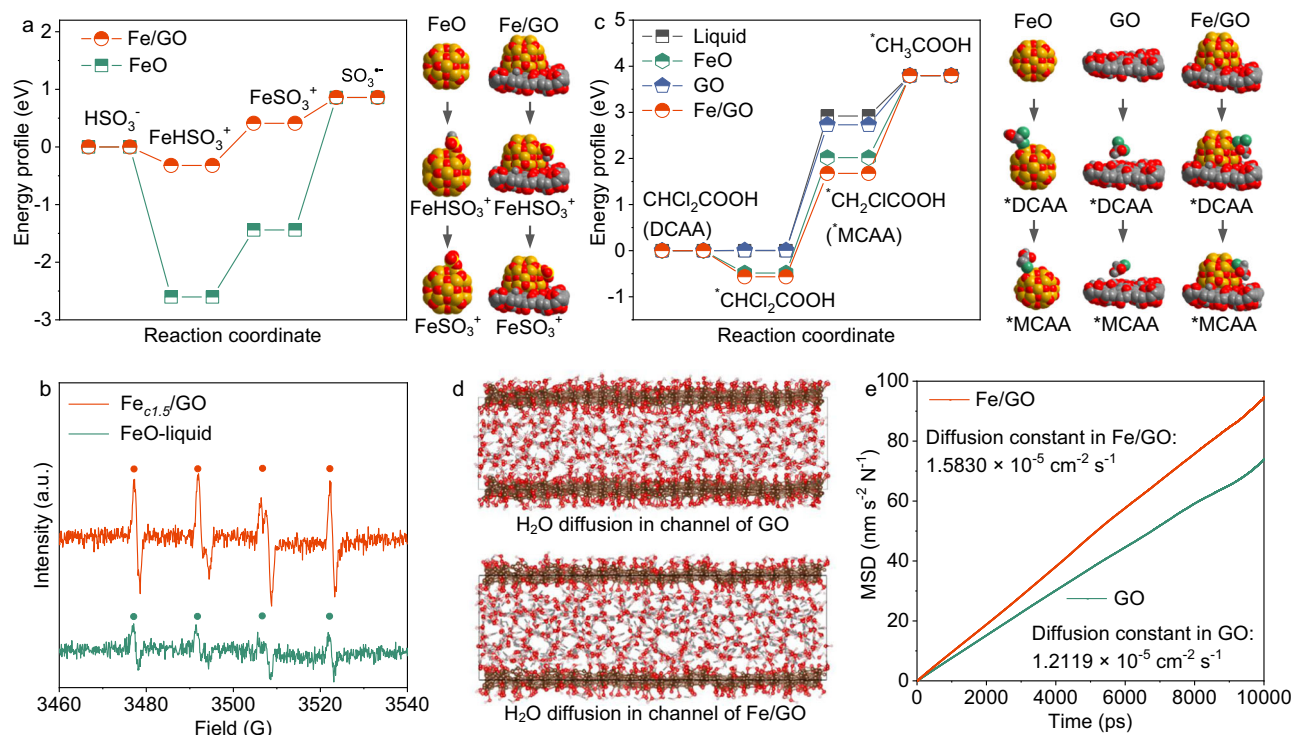


Fig. 4 | Calculated reaction mechanism of confinement catalysis and superior permeability. **a** Energy profiles of S(IV) dissociation through Fe/GO and FeO. Chemical structures of FeO, FeHSO₃⁺, and FeSO₃⁺ are presented in the first column, while Fe/GO, FeHSO₃⁺, and FeSO₃⁺ are displayed in the second column. **b** EPR spectra of the 5,5-dimethyl-1-pyrrolidine-N-oxide (DMPO) spin-trapping for Fe_{c1.5}/GO membrane catalytic systems and FeO/S(IV) bulk solutions. Circle symbols indicate signals of the DMPO/SO₃⁻ adduct. a. u. represents arbitrary unit. Conditions: DMPO concentration = 100 mM, initial S(IV) level = 1.0 mM, FeO dosage = 1.0 g L⁻¹, pH_{ini} 7.0 ± 0.1, and 25 ± 0.5 °C. **c** Energy profiles of DCAA degradation in Fe/GO, FeO, GO, and a free environment in the presence of S(IV). In the first column, the structures are presented for FeO, DCAA, and MCAA bound to FeO. In the second column, the structures are displayed for GO, DCAA, and MCAA bound to rGO. In the third column, the structures of Fe/GO, DCAA, and MCAA bound to Fe/GO are presented. **d**, **e** Diffusion of H₂O in interlayer channels of GO and Fe/GO. The orange line and green line represent Fe/GO and GO, respectively.

membranes exhibit a permeance of 48.6 L m⁻² h⁻¹ bar⁻¹, which is quadrupled compared to that of GO. In addition, the Fe/GO membranes display excellent stability and maintain their performance over 20 cycles. We have further demonstrated that the membranes are applicable for environmentally relevant concentrations and for a wide range of halogenated organic pollutants. Although the efficiency may be further improved by tuning chemical compositions, controlling nanoparticles and membrane structures, and applying other types of nanosheets and nanoparticles, the concept of designing catalytic membranes based on nanoparticles and two-dimensional nanosheets paves the way for enabling strong nanoconfinement effects for efficient dehalogenation and water treatment.

Methods

Materials and chemicals

MCAA (anhydrous, 99.0%), MBAA (anhydrous, ≥99.0%), DCAA (anhydrous, ≥99.0%), TCAA (anhydrous, ≥99.0%), DCA (anhydrous, 99.8%), TCA (97%), and FeCl₃ (anhydrous, 98.0%) were purchased from Sigma-Aldrich (USA). Graphite powder (99.0%), sodium sulfite (Na₂SO₃, ≥98.0%), sodium sulfate (Na₂SO₄, ≥99.0%), and sodium borohydride (NaBH₄, 98.0%) were purchased from Sinopharm Chemical Reagent Co. Ltd. (Shanghai, China). The 5,5-dimethyl-1-pyrrolidine-N-oxide (DMPO, ≥97.0 wt%) was obtained from Aladdin Chemistry Co. Ltd. (Shanghai, China). All chemicals were at least of analytical grade and used as received. Hydrophilic polyvinylidene difluoride membrane with 0.22 μm pore size was obtained from Merck (New Jersey, USA). All solutions were prepared in Milli-Q ultrapure water (18.2 MΩ cm, Millipore).

Fabrication of Fe/GO membranes

GO was prepared by oxidizing natural graphite powder using the Hummers method^{50–52}. Graphite powder (2.0 g) and NaNO₃ (1.0 g) were added in concentrated H₂SO₄ (48 mL) and the temperature was controlled using an ice bath. Then, KMnO₄ (6.0 g) was slowly added under stirring to prevent the temperature from exceeding 20 °C. After reaction for 2 hrs, the suspension was thermally treated at 35 °C for 1 h. Water (92 mL) was slowly added in the suspension, following by heat-treatment at 98 °C for 40 min and addition of 30% H₂O₂ solution. Ultimately, the product was washed with dilute HCl solution, collected, and dried. Colloidal dispersions of individual GO sheets in water (150 mL, 20 mg L⁻¹) were prepared using an ultrasonic homogenizer (JY98-IIIDN, Scientz) with ultrasound treatment at 40% power for 2 hrs. A solution of ferric iron ions (20 mL, 0.5–1.5 mmol L⁻¹) was prepared and added to the GO dispersion (150 mL, 20 mg L⁻¹). After adsorption for 10 hrs, the mixture was reduced by adding NaBH₄ in a controlled amount (i.e., 1.6 M, 75 μL). Subsequently, Fe/GO membranes were fabricated by vacuum filtration of the mixed solution (20.0 mL) under a vacuum pressure (0.95 bar). The membranes were then dried overnight at room temperature before further application. The resulting Fe/GO membranes were cut into rectangular strips of about 30 mm × 100 mm for testing, without any additional modification. Notably, excessively thin membranes (i.e., 80 μg GO) resulted in reduced removal efficiency, while excessively thick membranes (i.e., 1600 μg GO) led to decreased water permeance (Supplementary Fig. 17). Therefore, the membranes with moderate thickness (i.e., 400 μg GO) that was loaded with Fe NPs were selected in our study to achieve both high water permeance and excellent removal efficiency.

Characterization

The morphology of Fe/GO membranes was characterized using a STEM (Talos F200X STEM, Thermo Scientific) operating at 200 kV. To capture the TEM images of nanosheets, a TEM (JEM-2100, JEOL Ltd.) with an accelerating voltage of 200 kV was employed. For sample preparation, the GO or Fe/GO suspension was drop-cast onto a copper mesh-supported carbon film and dried at room temperature. The morphology and elemental distribution of the fabricated membranes were observed using a field-emission scanning electron microscope (SEM, Hitachi S-4800, Germany) with an accelerating voltage of 5 kV, equipped with an energy-dispersive spectrometer. To minimize the recharging effect and facilitate membrane sample preparation, the membrane was fractured in liquid nitrogen and subsequently coated with an ultrathin platinum layer. To investigate the nanosheet configuration and structure, an AFM (Multimode nanoscope, Bruker, USA) was utilized. NanoScope Analysis software was used to analyze images and height profiles. For sample preparation, the GO or Fe/GO suspension was drop-cast onto a mica plate and dried at room temperature. Furthermore, an XPS was carried out using an RBD (RBD Enterprises, USA) upgraded PHI-5000C ESCA system (Perkin Elmer) with monochromatic Mg K α X-rays ($h\nu = 1253.6$ eV) at 250 W. To ensure sufficient sensitivity and resolution, the high voltage was maintained at 14.0 kV, the pass energy was set to 46.95 eV, and the pressure in the analysis chamber was kept below 5×10^{-8} Pa. To measure the interlayer space of the membranes, an XRD (D8 Advance, Bruker Co.) with Cu K α radiation ($\lambda = 0.154056$ nm) was used in a continuous scanning mode. For dry samples, the membrane was dried at 50 °C before measurement. For wetted samples, the membrane was immersed in water for 1 h before measurement. The interlayer space was calculated using Bragg's Law of $2d\sin\theta = n\lambda$, where d and θ were the interlayer space and characteristic peak theta angle, respectively; and λ and n were 0.154056 nm and 1, respectively. Raman spectra were collected using a WITec micro-Raman at a 532 nm laser. The dynamic contact angle of the prepared membranes was recorded using an optical contact angle and interface tension meter (ST200KB, USA KINO Industry Co.).

Concentrations of haloacetic acids (i.e., MCAA, MBAA, DCAA, and TCAA) and their products (i.e., Cl $^-$ and Br $^-$) were quantified by an ion chromatograph (Dionex Aquion RFIC). A Dionex AS19 analytical column (4 \times 250 mm) and an AG19 guard column (4 \times 50 mm) were applied to separate them. Potassium hydroxide (20 mM) was used as effluents. Also, the measurement was carried out at a flow rate of 1.0 mL min $^{-1}$, a constant suppressor current of 50 mA, column temperature at 30 °C, and a duration of ~20 min. Prior to ion chromatography analysis, all the samples were filtered using a 0.22 μ m filter (Nylon, Titan). Concentrations of chlorinated organic pollutants (i.e., DCA and TCA) were analyzed by gas chromatograph using an electron capture detector (6820, Agilent). The analysis was performed under the column temperature of 100 °C and hydrogen flow rate of 1.5 mL min $^{-1}$. Elemental analyses, including iron concentrations, were performed by inductively coupled plasma mass spectrometry (ICP-MS, Agilent 7500 s). The detection limit for Fe was 1.0 μ g L $^{-1}$. Solution pH was determined at room temperature using a pH meter (MM374, Hach) calibrated with standard buffers routinely at pH 4.01, 7.01, and 10.01 prior to measurements. Moreover, electron paramagnetic resonance (EPR) experiments were carried out by using a JEOL FA200 EPR spectrometer with DMPO as a spin-trapping agent. All the EPR spectra were obtained at room temperature with a center field of 3350 Gs, a sweep width of 100 Gs, a 9.4 GHz microwave with a power of 1.0 mW, a modulation amplitude of 0.3 Gs, and a sweep time of 41.96 s. The concentration of DMPO, sulfite, and FeO as well as solution pH were 100 mM, 1.0 mM, 1.0 g L $^{-1}$, and 7.0 \pm 0.1, respectively, in all EPR analyses. The hyperfine splitting constants (i.e., a_N and $a_{\beta-H}$) related to peak distances were utilized to identify radicals.

Oxanyon reduction experiments

The performance of Fe/GO membranes for DCAA reduction was conducted using a laboratory-scale cross-flow membrane test system. The schematic of the filtration system with all components including recirculation is shown in Supplementary Fig. 18 of the Supporting Information^{53,54}. Each membrane coupon was installed in a cross-flow cell (CF042, Sterlitech) with an effective area of 8.0 cm 2 . During catalytic filtration experiments, the stock solution containing sulfite (i.e., 1 mM S(IV)) and haloacetic acids (i.e., 80 or 180 μ g L $^{-1}$ MCAA, MBAA, DCAA, and TCAA) or chlorinated organic pollutants (i.e., 0.5 mM DCA and TCA) was prepared, and then it has been utilized as the feed to the reaction membrane module under a flow rate of about 0.2 L min $^{-1}$, a pressure of 1.0–2.0 bar, and 90% of power. Unless specified otherwise, all the catalytic filtration tests were performed with only the retentate recirculated back to the feed tank, as presented in Supplementary Fig. 18. To ensure this recirculation does not affect the oxanyon removal performance, additional catalytic filtration tests without recirculation were also included for comparison in Supplementary Fig. 19. For the long-term performance testing of Fe/GO membrane catalytic systems, the feed solution, including S(IV) and haloacetic acids, was replenished with a solution volume of 50–100 mL at regular intervals of 1.0 h between cycles; each cycle represents at least 50–100 mL of clean permeate water obtained by membrane catalytic systems. After the catalytic filtration experiment, the permeate was collected at predetermined sampling time (i.e., 2, 5, 10, 20, 30, and 60 min), and immediately analyzed for halogenated organics reduction, product formation, and iron leaching. All the experiments were carried out at room temperature. It is worthwhile to note that the shortest sampling time was 2 min in the current study due to the time needed for the permeate water to reach to the sampling point.

In addition, in suspension systems containing Fe_{CLS}/GO composites/S(IV), reduction reactions were initiated by introducing DCAA, Fe_{CLS}/GO composites, and S(IV) into the solutions. Stock solutions of Na₂SO₃ were freshly prepared prior to each set of experiments. Samples were withdrawn at predetermined time of 0, 0.5, 1, 2, 3, 4, 6, and 8 hrs, and the residual S(IV) in the samples was quenched by adding H₂O₂.

Reaction kinetics model

The retention time can be calculated by Eq. 1:

$$t = \frac{V}{Q} = \frac{S \times h}{J \times S \times P} = \frac{h}{J \times P} \quad (1)$$

Where V is the pore volume of membrane (cm 3), Q is the flow rate (mL min $^{-1}$), S (m 2) is the effective membrane filtration area, h (nm) is the effective thickness of interlayer free space, and J (L m $^{-2}$ h $^{-1}$ bar $^{-1}$) and P (bar) are water permeance and applied pressure, respectively.

Additionally, the observed rate constants (k) for DCAA reduction were calculated based on the pseudo-first-order kinetics model shown in Eq. 2, where r is the rate of DCAA reduction (μ g min $^{-1}$), C_{DCAA} represents DCAA concentration (μ g), and t indicates retention time, i.e., the hydraulic residence time within the catalytic membrane (min).

$$r = \frac{-dC_{DCAA}}{dt} = kC_{DCAA} \quad (2)$$

Computational methods

Molecular dynamics simulations were performed using the GROMACS software package (version 2021.3)^{55–57}. The systems containing GO and rGO with different C:O ratios and layer distances were constructed using the gmxttools software⁵⁸, and the SPC water model was filled into the GO and rGO systems⁵⁹. The atomic interactions in GO and rGO were parameterized using the general AMBER force field (GAFF)⁶⁰. After

energy minimization, production runs were carried out in the NVT ensemble at 300 K with a time step of 1 fs. The system temperature was controlled using a v-rescale thermostat ($\tau_T=1$ ps). After 10 ns of simulation, the mean squared displacement (MSD) of the water molecules was analyzed by using the GROMACS toolkits.

Moreover, we calculated the free energy diagram of the conversion from HSO_3^- to SO_3^{2-} and from DCAA to CAA in Fe/GO, FeO, rGO, and a free environment in the presence of S(IV) by using the CP2K package (version 2023) in the framework of the density functional theory⁶¹, according to the hybrid Gaussian and plan-wave scheme⁶². The molecular orbitals of the valence electrons were expanded into DZVP-MOLOPT-SR-GTH basis sets⁶³, while atomic core electrons were described using Goedecker-Teter-Hutter (GTH) pseudopotentials⁶⁴. A plane-wave density cutoff of 500 Ry was adopted. The long-range van der Waals interactions have been described by the DFT-D3 approach²³. All the structures were fully relaxed using the BFGS scheme in CP2K, and the force convergence criterion was set to 4.5×10^{-4} hartree bhor⁻¹. In the calculations of FeO in a liquid environment, the energies were calibrated using the SCCS continuum solvation model^{65–67}.

Statistical analysis

Experiments were repeated at least three times, and error bars represent \pm one standard deviation from the mean of the independent triplicates. Student's *t*-test (two-tailed, unpaired, assuming equal variance) was used to determine if differences in oxyanion removal kinetics were significant (e.g., $p < 0.05$).

Data availability

The data supporting the findings of this study are included in the main text and supplementary information filed. Additional data are available from the corresponding author upon request. Source data are provided with this paper.

References

- Sinha, R., Gupta, A. K. & Ghosal, P. S. A review on Trihalomethanes and Haloacetic acids in drinking water: global status, health impact, insights of control and removal technologies. *J. Environ. Chem. Eng.* **9**, 106511 (2021).
- Zhao, X., Li, A., Mao, R., Liu, H. & Qu, J. Electrochemical removal of haloacetic acids in a three-dimensional electrochemical reactor with Pd-GAC particles as fixed filler and Pd-modified carbon paper as cathode. *Water Res.* **51**, 134–143 (2014).
- Dettori, M., Arghittu, A., Deiana, G., Castiglia, P. & Azara, A. The revised European directive 2020/2184 on the quality of water intended for human consumption. A step forward in risk assessment, consumer safety and informative communication. *Environ. Res.* **209**, 112773 (2022).
- IARC. International Agency for Research on Cancer. <https://www.iarc.who.int/research-home/> (2024).
- Agency, USEP. Public Notification - Total Trihalomethanes (TTHM) and Haloacetic Acids (HAA5) MCL Template. <https://www.epa.gov/region8-waterops/public-notification-total-trihalomethanes-tthm-and-haloacetic-acids-haa5-mcl>. (2024).
- Yao, Q. et al. Amorphous nickel phosphide as a noble metal-free cathode for electrochemical dechlorination. *Water Res.* **165**, 114930 (2019).
- Mao, R. et al. Insights into co-removal of trichloroacetic acid and bromate by an electroreduction process: competitive reaction mechanism and enhanced atomic H⁺ stabilization. *Chem. Eng. J.* **429**, 132139 (2022).
- Zhang, L., Ai, W., Li, C., Zhang, Q. & Li, T. Efficient photolytic degradation of disinfection by-products by using a high photon flux UV system: monochloroacetic acid, dichloroacetic acid and trichloroacetic acid. *Water Supply* **18**, 2063–2070 (2018).
- Zhang, J., Zhang, H., Liu, X., Cui, F. & Zhao, Z. Efficient reductive and oxidative decomposition of haloacetic acids by the vacuum-ultra-violet/sulfite system. *Water Res.* **210**, 117974 (2022).
- Wang, L., Chen, Y., Chen, B. & Yang, J. Generation of hydroxyl radicals during photodegradation of chloroacetic acids by 254 nm ultraviolet: A special degradation process revealed by a holistic radical determination methodology. *J. Hazard. Mater.* **404**, 124040 (2021).
- Zhang, L., Arnold, W. A. & Hozalski, R. M. Kinetics of haloacetic acid reactions with Fe(O). *Environ. Sci. Technol.* **38**, 6881–6889 (2004).
- Guo, B. et al. Ultra-fast catalytic hydrodechlorination of chloroacetic acids over Pd catalyst supported on CeO₂ with exposed (110) plane. *Chem. Eng. J.* **472**, 145126 (2023).
- Hozalski, R. M., Zhang, L. & Arnold, W. A. Reduction of haloacetic acids by Fe⁰: implications for treatment and fate. *Environ. Sci. Technol.* **35**, 2258–2263 (2001).
- Xiao, Q. et al. An overview of advanced reduction processes for bromate removal from drinking water: Reducing agents, activation methods, applications and mechanisms. *J. Hazard Mater.* **324**, 230–240 (2017).
- Xiao, Q. & Yu, S. Reduction of bromate from drinking water by sulfite/ferric ion systems: efficacy and mechanisms. *J. Hazard Mater.* **418**, 125940 (2021).
- Xiao, Q. & Yu, S. The role of dissolved oxygen in the sulfite/divalent transition metal ion system: degradation performances and mechanisms. *Chem. Eng. J.* **417**, 129115 (2021).
- Xiao, Q., Ren, Y. & Yu, S. Pilot study on bromate reduction from drinking water by UV/sulfite systems: economic cost comparisons, effects of environmental parameters and mechanisms. *Chem. Eng. J.* **330**, 1203–1210 (2017).
- Xiao, Q., Wang, T., Yu, S., Yi, P. & Li, L. Influence of UV lamp, sulfur(IV) concentration, and pH on bromate degradation in UV/sulfite systems: Mechanisms and applications. *Water Res.* **111**, 288–296 (2017).
- Liu, X., Vellanki, B. P., Batchelor, B. & Abdel-Wahab, A. Degradation of 1,2-dichloroethane with advanced reduction processes (ARPs): effects of process variables and mechanisms. *Chem. Eng. J.* **237**, 300–307 (2014).
- Yazdanbakhsh, A., Eslami, A., Moussavi, G., Rafiee, M. & Sheikhmohammadi, A. Photo-assisted degradation of 2, 4, 6-trichlorophenol by an advanced reduction process based on sulfite anion radical: degradation, dechlorination and mineralization. *Chemosphere* **191**, 156–165 (2018).
- Zhou, D., Chen, L., Li, J. & Wu, F. Transition metal catalyzed sulfite auto-oxidation systems for oxidative decontamination in waters: a state-of-the-art minireview. *Chem. Eng. J.* **346**, 726–738 (2018).
- Kraft, J. & Van Eldik, R. Kinetics and mechanism of the iron (III)-catalyzed autoxidation of sulfur (IV) oxides in aqueous solution. 1. Formation of transient iron (III)-sulfur (IV) complexes. *Inorg. Chem.* **28**, 2297–2305 (1989).
- Grimme, S., Antony, J., Ehrlich, S. & Krieg, H. A consistent and accurate ab initio parametrization of density functional dispersion correction (DFT-D) for the 94 elements H–Pu. *J. Chem. Phys.* **132**, 154104 (2010).
- Zhang, Y., Zhou, J., Li, C., Guo, S. & Wang, G. Reaction kinetics and mechanism of iron(II)-induced catalytic oxidation of sulfur(IV) during wet desulfurization. *Ind. Eng. Chem. Res.* **51**, 1158–1165 (2012).
- Ogbonna, C. N. & Nwoba, E. G. Bio-based flocculants for sustainable harvesting of microalgae for biofuel production. A review. *Renew. Sustain. Energy Rev.* **139**, 110690 (2021).
- Long, Y. et al. Sulfur-containing iron nanocomposites confined in S/N co-doped carbon for catalytic peroxymonosulfate oxidation of organic pollutants: low iron leaching, degradation mechanism and intermediates. *Chem. Eng. J.* **404**, 126499 (2021).

27. Zhang, S. et al. Membrane-confined iron oxychloride nanocatalysts for highly efficient Heterogeneous Fenton water treatment. *Environ. Sci. Technol.* **55**, 9266–9275 (2021).
28. Xie, J. et al. Sequential ultrafiltration-catalysis membrane for excellent removal of multiple pollutants in water. *Environ. Sci. Technol.* **55**, 2652–2661 (2021).
29. Wu, X. et al. Single-atom cobalt incorporated in a 2D graphene oxide membrane for catalytic pollutant degradation. *Environ. Sci. Technol.* **56**, 1341–1351 (2022).
30. Ma, W. et al. Catalytic membrane with copper single-atom catalysts for effective hydrogen peroxide activation and pollutant destruction. *Environ. Sci. Technol.* **56**, 8733–8745 (2022).
31. Ozdemir, S., Buonomenna, M. & Drioli, E. Catalytic polymeric membranes: preparation and application. *Appl. Catal. A. Gen.* **307**, 167–183 (2006).
32. Li, N. et al. Catalytic membrane-based oxidation-filtration systems for organic wastewater purification: a review. *J. Hazard Mater.* **414**, 125478 (2021).
33. Li, C., Sun, W., Lu, Z., Ao, X. & Li, S. Ceramic nanocomposite membranes and membrane fouling: A review. *Water Res.* **175**, 115674 (2020).
34. Dong, X., Jin, W., Xu, N. & Li, K. Dense ceramic catalytic membranes and membrane reactors for energy and environmental applications. *Chem. Commun.* **47**, 10886–10902 (2011).
35. Pei, S. & Cheng, H.-M. The reduction of graphene oxide. *Carbon* **50**, 3210–3228 (2012).
36. Zhang, W. et al. General synthesis of ultrafine metal oxide/reduced graphene oxide nanocomposites for ultrahigh-flux nanofiltration membrane. *Nat. Commun.* **13**, 471 (2022).
37. Chua, C. K. & Pumera, M. Chemical reduction of graphene oxide: a synthetic chemistry viewpoint. *Chem. Soc. Rev.* **43**, 291–312 (2014).
38. Kudin, K. N. et al. Raman spectra of graphite oxide and functionalized graphene sheets. *Nano Lett.* **8**, 36–41 (2008).
39. Meng, C. et al. Angstrom-confined catalytic water purification within Co-TiOx laminar membrane nanochannels. *Nat. Commun.* **13**, 4010 (2022).
40. Zhang, W. L. & Choi, H. J. Silica-graphene oxide hybrid composite particles and their electroresponsive characteristics. *Langmuir* **28**, 7055–7062 (2012).
41. Willcox, J. L. & Kim, H. J. Molecular dynamics study of water flow across multiple layers of pristine, oxidized, and mixed regions of graphene oxide. *ACS Nano* **11**, 2187–2193 (2017).
42. Moussavi, G. & Rezaei, M. Exploring the advanced oxidation/reduction processes in the VUV photoreactor for dechlorination and mineralization of trichloroacetic acid: parametric experiments, degradation pathway and bioassessment. *Chem. Eng. J.* **328**, 331–342 (2017).
43. Liu, Y. et al. Reductive dechlorination of trichloroacetic acid (TCAA) by electrochemical process over Pd-In/Al₂O₃ catalyst. *Electrochim. Acta* **232**, 13–21 (2017).
44. Yang, E. et al. Tunable semi-permeability of graphene-based membranes by adjusting reduction degree of laminar graphene oxide layer. *J. Membr. Sci.* **547**, 73–79 (2018).
45. Dong, H., Wei, G., Yin, D. & Guan, X. Mechanistic insight into the generation of reactive oxygen species in sulfite activation with Fe(III) for contaminants degradation. *J. Hazard Mater.* **384**, 121497 (2020).
46. Dong, H. et al. Reinvestigating the role of reactive species in the oxidation of organic co-contaminants during Cr(VI) reactions with sulfite. *Chemosphere* **196**, 593–597 (2018).
47. Li, W., Wu, W. & Li, Z. Controlling interlayer spacing of graphene oxide membranes by external pressure regulation. *ACS Nano* **12**, 9309–9317 (2018).
48. Shen, J., Liu, G., Han, Y. & Jin, W. Artificial channels for confined mass transport at the sub-nanometre scale. *Nat. Rev. Mater.* **6**, 294–312 (2021).
49. Saraswat, V. et al. Invariance of water permeance through size-differentiated graphene oxide laminates. *ACS Nano* **12**, 7855–7865 (2018).
50. Kim, S. et al. Room-temperature metastability of multilayer graphene oxide films. *Nat. Mater.* **11**, 544–549 (2012).
51. Eda, G., Fanchini, G. & Chhowalla, M. Large-area ultrathin films of reduced graphene oxide as a transparent and flexible electronic material. *Nat. Nanotechnol.* **3**, 270–274 (2008).
52. Dikin, D. A. et al. Preparation and characterization of graphene oxide paper. *Nature* **448**, 457–460 (2007).
53. Peng, L. E., Yao, Z., Chen, J., Guo, H. & Tang, C. Y. Highly selective separation and resource recovery using forward osmosis membrane assembled by polyphenol network. *J. Membr. Sci.* **611**, 118305 (2020).
54. Yang, Z. et al. Mechanistic insights into the role of polydopamine interlayer toward improved separation performance of polyamide nanofiltration membranes. *Environ. Sci. Technol.* **54**, 11611–11621 (2020).
55. Van Der Spoel, D. et al. GROMACS: Fast, flexible, and free. *J. Comput. Chem.* **26**, 1701–1718 (2005).
56. Abraham, M. J. et al. GROMACS: High performance molecular simulations through multi-level parallelism from laptops to supercomputers. *SoftwareX* **1–2**, 19–25 (2015).
57. Berendsen, H. J., Spoel, D. V. D. & Drunen, R. V. GROMACS: A message-passing parallel molecular dynamics implementation. *Comput. Phys. Commun.* **91**, 43–56 (1995).
58. Li, J. The gmxtools software. *Zenodo* <https://doi.org/10.5281/zenodo.6408973> (2022).
59. Berendsen, H. J. C., Grigera, J. R. & Straatsma, T. P. The missing term in effective pair potentials. *J. Phys. Chem.* **91**, 6269–6271 (1987).
60. Wang, J., Wolf, R. M., Caldwell, J. W., Kollman, P. A. & Case, D. A. Development and testing of a general amber force field. *J. Comput. Chem.* **25**, 1157–1174 (2004).
61. Hutter, J., Iannuzzi, M., Schiffrmann, F. & Vandevondele, J. cp2k: atomistic simulations of condensed matter systems. *Wiley Interdiscip. Rev. Comput. Mol. Sci.* **4**, 15–25 (2014).
62. Lippert, B. G., Parrinello, J. H. & Michele, A. hybrid Gaussian and plane wave density functional scheme. *Mol. Phys.* **92**, 477–488 (2010).
63. Vandevondele, J. & Hutter, J. Gaussian basis sets for accurate calculations on molecular systems in gas and condensed phases. *J. Chem. Phys.* **127**, 114105 (2007).
64. Goedecker, S., Teter, M. & Hutter, J. Separable dual-space Gaussian pseudopotentials. *Phys. Rev. B* **54**, 1703 (1996).
65. Andreussi, O., Dabo, I. & Marzari, N. Revised self-consistent continuum solvation in electronic-structure calculations. *J. Chem. Phys.* **136**, 064102 (2012).
66. Fattbert, J. L. & Gygi, F. Density functional theory for efficient ab initio molecular dynamics simulations in solution. *J. Comput. Chem.* **23**, 662–666 (2002).
67. Yin, W.-J., Krack, M., Li, X., Chen, L.-Z. & Liu, L.-M. Periodic continuum solvation model integrated with first-principles calculations for solid surfaces. *Prog. Nat. Sci. Mater. Int.* **27**, 283–288 (2017).

Acknowledgements

This work was substantially supported by NSFC-RGC Funding Scheme (N_HKU721/22 to C.T.) from the Research Grants Council of the Hong Kong Special Administration Region, China. The research was also sponsored by the Hong Kong Scholar Program (No. XJ2021035 to Q.X.), and the Shanghai Pujiang Program (No. 22PJ075 to Q.X.). We appreciate the staff from the Electron Microscope Unit of The University of Hong Kong for SEM and TEM sample preparation and analysis. We thank the high-performance public computing service platform of Jinan University for providing computational resources.

Author contributions

Q.X., W.L., and C.T. conceived the idea and designed the research. Q.X. S.X., and L.W. performed the research. Q.X., W.L., and C.T. interpreted the data and wrote the manuscript.

Competing interests

The authors declare no competing interests.

Additional information

Supplementary information The online version contains supplementary material available at <https://doi.org/10.1038/s41467-024-54055-x>.

Correspondence and requests for materials should be addressed to Wanbin Li or Chuyang Y. Tang.

Peer review information *Nature Communications* thanks the anonymous reviewers for their contribution to the peer review of this work. A peer review file is available.

Reprints and permissions information is available at <http://www.nature.com/reprints>

Publisher's note Springer Nature remains neutral with regard to jurisdictional claims in published maps and institutional affiliations.

Open Access This article is licensed under a Creative Commons Attribution 4.0 International License, which permits use, sharing, adaptation, distribution and reproduction in any medium or format, as long as you give appropriate credit to the original author(s) and the source, provide a link to the Creative Commons licence, and indicate if changes were made. The images or other third party material in this article are included in the article's Creative Commons licence, unless indicated otherwise in a credit line to the material. If material is not included in the article's Creative Commons licence and your intended use is not permitted by statutory regulation or exceeds the permitted use, you will need to obtain permission directly from the copyright holder. To view a copy of this licence, visit <http://creativecommons.org/licenses/by/4.0/>.

© The Author(s) 2024